BIOSYSTEMS ENGINEERING 223 (2022) 277–294

Available online at www.sciencedirect.com

ScienceDirect

journal homepage: www.elsevier.com/locate/issn/15375110

Research Paper

Bed expansion at backwashing in pressurised porous media filters for drip irrigation: Numerical simulations and analytical equations

Jonathan Graciano-Uribe [a,*], *Toni Pujol* [b,**], *Diego Hincapie-Zuluaga* [a], *Jaume Puig-Bargués* [c], *Miquel Duran-Ros* [c], *Gerard Arbat* [c], *Francisco Ramírez de Cartagena* [c]

[a] *Department of Mechatronics and Electromechanics, Faculty of Engineering, Metropolitan Institute of Technology, Bloque E Campus Robledo, 050036 Medellín, Colombia*

[b] *Department of Mechanical Engineering and Industrial Construction, University of Girona, c/ Universitat de Girona 4, 17003 Girona, Catalonia, Spain*

[c] *Department of Chemical and Agricultural Engineering and Technology, University of Girona, c/ Maria Aurèlia Capmany 61, 17003 Girona, Catalonia, Spain*

ARTICLE INFO

Article history:
Received 14 March 2022
Received in revised form
8 September 2022
Accepted 22 September 2022
Published online xxx

Keywords:
Backwashing
Fluidisation
Granular bed
Micro-irrigation
Computational fluid dynamics

Actions for improving the energy efficiency of pressurised porous media filters used in drip micro-irrigation require methods to properly determine the behaviour of both filtration and backwashing modes. The latter is essentially a fluidisation process. Though many authors have analysed fluidised bed columns, very few studies have dealt with the backwashing of granular media filters used in agriculture. The purpose of the present work was 1) to validate a computational fluid dynamics (CFD) model to simulate the backwashing regime, and 2) to assess the extent of analytical expressions for determining the expanded bed height. Experimental data were obtained using a laboratory filter for two types of porous media at superficial velocities <150 m h^{-1}. The CFD model used the Eulerian–Eulerian approach, and its sensitivity was investigated in a simplified two-dimensional domain. A modified three-dimensional model effectively reproduced the bed expansion for most of the experimental conditions using large time steps (0.025 s) and few internal iterations (20). Well-known analytical equations overestimated the expanded bed height at superficial velocities <150 m h^{-1}, but the recent RIO 1 model proposed by Kramer et al. (2020) showed very good predictive capacities. Two analytical expressions based on basic principles were developed, providing a trend which was also close to observations and a lower bound for the expanded bed height value. These conclusions were confirmed by analysing external data obtained using commercial pressurised sand filters.

* Corresponding author.
** Corresponding author.
E-mail addresses: jonathangraciano@itm.edu.co (J. Graciano-Uribe), toni.pujol@udg.edu (T. Pujol).

https://doi.org/10.1016/j.biosystemseng.2022.09.008

Nomenclature

A_f	Cross-sectional area of the filter body (mm^2)
AR_{max}	Maximum mesh aspect ratio value (–)
CFL	Courant–Friedrichs–Lewy number (–)
d_c	Water channel equivalent diameter (mm)
d_{eq}	Particle equivalent diameter (mm)
d_f	Filter inner diameter (mm)
d_p	Sauter mean diameter (mm; m in equations)
f	Friction factor (–)
f_L	Drag coefficient for the laminar regime (–)
Fr_p	Particle Froude number (–)
GC^{21}_{index}	Fine grid convergence index (%)
g	Acceleration of gravity (m s^{-2})
h	2D horizontal model width (mm)
K	Minor loss coefficient (–)
$k-\varepsilon$	Standard $k-\varepsilon$ turbulence model
L	Height of the granular bed (mm; m in equations)
L_r	Relative variation of L with respect to the no flow conditions (%)
N	Number of grains in water channel inside the media (–)
n	Number of experimental data (–)
NSE	Nash-Sutcliffe efficiency coefficient (–)
OQ_{min}	Minimum mesh orthogonal quality value (–)
P_h	Hydraulic power (W)
Q	Flow rate (m^3 s^{-1})
R^2	Coefficient of determination (–)
Re	Reynolds number (–)
Re_1	Modified Reynolds number (–)
Re_c	Reynolds number of water channel (–)
Re_ε	Modified particle Reynolds number (–)
RF	Reynolds-Froude parameter for RIO 1 model (–)
$RMSE$	Root mean square error of L_r (%)
S_{max}	Maximum mesh skewness value (–)
SD	Standard deviation of L_r data (%)
$SST\ k-\omega$	Shear stress transport $k-\omega$ turbulence model
u	Characteristic flow velocity (mm s^{-1})
v_c	Mean water channel velocity (m s^{-1})
v_s	Superficial velocity (m h^{-1}; m s^{-1} in equations)
$v_{s,min}$	Minimum fluidisation velocity (m h^{-1}; m s^{-1} in equations)
Δl	Grid cell size (mm)
Δp	Pressure drop (kPa, Pa in equations)
Δp_f	Major (friction) pressure drop in a water channel inside the media (Pa)
Δp_m	Minor pressure drop in a water channel inside the media (Pa)
Δt	Time step (s)
ε	Porosity (–)
μ	Fluid viscosity (Pa s)
ρ_f	Fluid density (kg m^{-3})
ρ_p	Particle density (kg m^{-3})
φ	Dimensionless group (–)
ψ	Particle sphericity coefficient (–)

Subscripts

0	Condition with flow at rest
i	ith value of data

1. Introduction

Short-term future scenarios predict changes in rainfall distribution that may compromise the freshwater availability in many regions (Schewe et al., 2014). The Mediterranean basin is one of these vulnerable areas, being especially sensitive to issues related to global change (IPCC, 2021). However, recent studies indicate that the adoption of mitigation actions can compensate current expected impacts (Jorda-Capdevila et al., 2019). Technological advances may ensure agricultural sustainability by means of improving energy efficiency and reducing water consumption (Fatih Isik, Sönmez, Yilmaz, Özdemir, & NurcanYilmaz, 2017; Martos, Ahmad, Cartujo, & Ordoñez, 2021).

Drip irrigation is a well-known technique focused on increasing crop productivity while decreasing water use (e.g., Zou et al., 2020). This irrigation method requires water filtration mechanisms to retain particles so as to not clog the emitters (Duran-Ros et al., 2021). The required amount of water flow is obtained with pumping units, so high energy consumption is one of the drawbacks of this technology (Garb & Friedlander, 2014).

Media filters are extensively used in drip irrigation systems (Burt, 2010). Essentially, these types of filters consist of a granular bed that retains particles (Pujol et al., 2020). As the particle retention in the sand column progresses, the pressure drop increases and so does the power requirements of the pumping unit (Solé-Torres et al., 2019). Once a threshold pressure drop value for the entire filter element has been reached, an automatic 3-way valve modifies the flow direction and the backflushing of the filter begins (Burt, 2010). This process may last more than 2 min during which the system behaves as a fluidised bed where particles are flushed out of the filter dragged by the backflow (Jiao, Feng, Liu, Yang, Hang, 2020).

Although the fluidisation process is a thoroughly investigated phenomenon due to its relevance in many industrial applications, few studies have analysed the hydraulics behaviour of the backwash regime in granular media filters commonly used in drip irrigation systems. de Deus, Testezlaf, and Mesquita (2016) analysed the backwashing performance of an irrigation commercial sand filter using three media particle sizes at an expansion regime whose total bed height was 25% longer than the initial one. This height was below the optimum one (≈100% bed height increase with respect to the initial value) in which the porosity of an expanded uniform media maximises the hydrodynamic shear forces over the grains thereby favouring the particle detachment. For a packed bed porosity of 0.4, this optimum regime is achieved at an expanded bed porosity ≈0.70 (Amirtharajah, 1971). The height increase of the optimum bed expansion is substantially lower for filters using non-uniform media (≈40% increase of

the bed height initial value (Amirtharajah, 1971)). In practice, however, reported data from water treatment plants suggest optimum backwashing regimes at bed expansions between 20% and 25% of the initial packed bed height (Amirtharajah, 1971), mainly due to sizing constraints of commercial filters as well as energy and water savings requirements (Brouckaert, 2004).

In filters for drip-irrigation systems, de Deus, Mesquita, Testezlaf, de Almeida, and de Oliveira (2020) proposed a methodology to experimentally measure the height of the expanded bed and to indirectly determine the pressure drop in the media, which was used to evaluate the minimum fluidisation velocity (threshold value of the upward superficial velocity above which the media expands). These authors applied this methodology to the study of three commercial sand filters working with three specific packed bed heights and three specific media (de Deus, Mesquita, Salcedo Ramirez, Testezlaf, & de Almeida, 2020). They found that the minimum fluidisation velocity was independent of the initial packed bed height but was an increasing function of the media particle size (de Deus, Mesquita, Salcedo Ramirez, et al., 2020). These results confirmed the theoretical behaviour based on the momentum conservation equation applied as an integral form in a control volume composed of the packed granular media (McCabe, Smith, & Harriott, 1993). In this calculation, the pressure change in the media is often expressed in terms of the Ergun equation (McCabe et al., 1993), which successfully predicts the pressure drop in filtration mode (Graciano-Uribe et al., 2021).

The granular bed expands and porosity rises when increasing the superficial velocity beyond the minimum fluidisation value. In an incipient fluidised bed regime, pressure drop equations like those of Ergun and, especially, Kozeny-Carman may be accepted, though quasi-analytical prediction equations are often based on developing an expression for the dimensionless friction factor to relate superficial velocity to porosity (Soyer & Akgiray, 2009). Indeed, the latter expression can be understood as a modification of the constant parameters in Ergun or Kozeny-Carman pressure drop equations so as to vary with the flow velocity (Kramer et al., 2021). The calculation of the height of the expanded bed is then obtained by applying the mass conservation equation since both the porosity and height of the initial packed bed are known.

The Dharmarajah and Cleasby (1986) bed expansion analytical model uses the above strategy and has extensively been used with very accurate predictions for spherical particles. However, some data indicate that, at incipient fluidisation, this model may tend to overestimate the slope of the bed expansion curve as a function of the superficial velocity (Clements & Haarhoff, 2005). In addition, the Dharmarajah and Cleasby (1986) model might not be accurate enough when working with non-spherical particles and some modifications have been proposed to generalise it (Soyer & Akgiray, 2009). Recently, Kramer et al. (2020) have developed several analytical equations to predict the expanded bed porosity focused on both laminar and transitional flow regimes with heterogeneous flow patterns and irregular spatial particle distributions. The final proposed equation was reported to achieve an average relative error lower than 1% in comparison with experimental voidage values.

Besides laboratory experiments and quasi-analytical models, the option of simulating the fluidisation process with computational fluid dynamics (CFD) is very attractive. A CFD tool may provide fast and accurate simulations to determine the operating conditions of filters in backwash mode. Therefore, CFD may successfully supplement laboratory experiments, especially at the initial stages of the product development where numerous design options may be under consideration.

However, the simulation of a fluidisation process is a complex problem that can be solved by applying different strategies. The simplest one corresponds to analysing the liquid–solid interaction with two phase flow models based on an Eulerian–Eulerian approach in which the granular material is defined in terms of a continuous phase (see, e.g., ANSYS Inc, 2021; Peng, Sun, Han, & Xie, 2021). Alternatively, the liquid–solid behaviour can also be analysed with an Eulerian-Lagrangian approach in which the media is treated as individual particles with the discrete element method (DEM), taking into account both particle–particle and particle–flow interactions (e.g., Hua, Lu, & Yang, 2020). Simulations of liquid–solid fluidisation processes are less common than those for gas–solid systems (≈1/7.5 ratio with keywords "fluidised bed" + "CFD" + "liquid–solid" or "solid–liquid" vs "gas–solid" or "solid–gas" in a Web of Science search). Moreover, in the liquid–solid fluidisation topic, there were no references that simulated conditions typically found in pressurised media filters employed in drip irrigation systems.

Therefore, the purpose of the present work was: 1) to validate a CFD methodology able to simulate the fluidisation process, and 2) to analyse the validity of analytical equations to predict the granular bed expansion of standard filters used in drip micro-irrigation.

2. Materials and methods

2.1. Experimental set up.

The experimental set up consisted of a closed circuit system (Fig. 1). A 100 l capacity tank supplied water to a centrifugal pump (Prisma 20/4 M, ESPA, Banyoles, Spain). A water meter (405 S DN15, Sensus, Badalona, Spain) was installed at the discharge pipe. In the backwashing configuration, this pipe was connected to the bottom inlet of a filter manufactured with polymethyl methacrylate acrylic plastic (PMMA) to allow the visualisation of the fluidisation process. The main dimensions of the filter are detailed in Fig. 2. The porous media was supported and retained by two circular sheets of stainless steel screen with a 0.125 mm sieve opening whose diameter was equal to that of the inner filter. These two sheets were packed between an upper stainless steel perforated plate (0.8 mm hole diameter) bolted to a lower cylindrical PMMA element. The latter had an open area equal to 5275 mm^2, being smaller than the cross-sectional area of the filter main body ($A_f = 9503$ mm^2 since the filter inner diameter was $d_f = 0.110$ m) due to the existence of radial reinforcement arms (see Fig. 2). The diffuser was fixed to the filter top cover. It consisted of a cylinder of 35 mm outer diameter with four equally distributed side openings, each one 8 mm in height and with a 19.5 mm arc length. The filter outlet located on the upper part

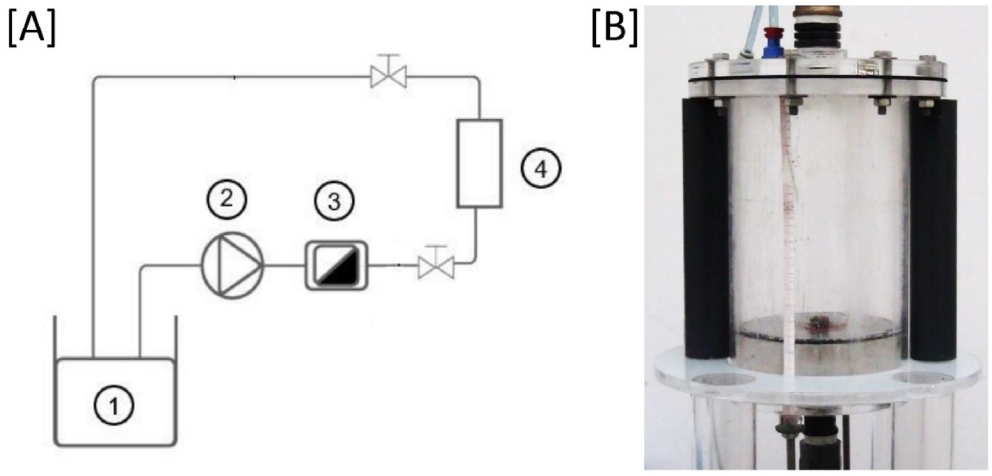

Fig. 1 – Schematic layout of the experimental set up [A] with water tank (1), centrifugal pump (2), water meter (3), and filter body (4), and picture of the laboratory experiment [B].

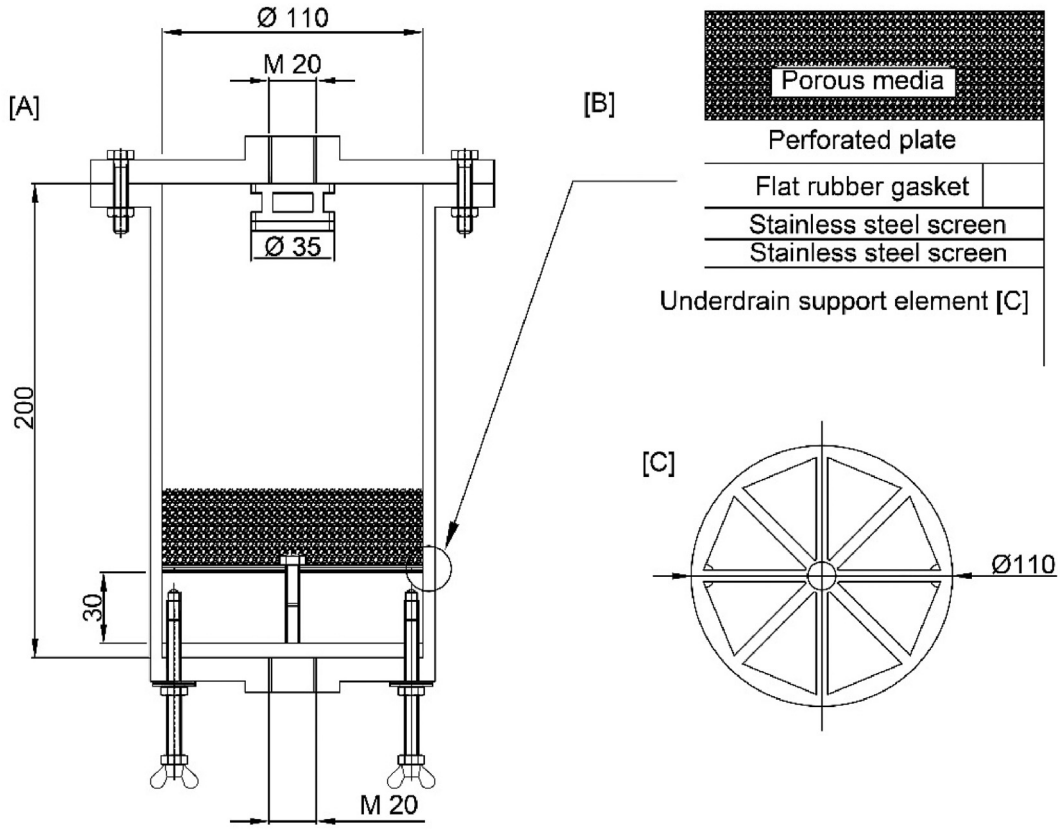

Fig. 2 – Main filter dimensions (units in mm) [A], detail of the underdrain zone [B], top view of the underdrain support element 30 mm high [C].

was connected to a return pipe back to the water tank. Pressure was limited to a conservative 200 kPa at the inlet to avoid damaging the PMMA body. The filter top cover had an air release valve to release air bubbles that could be trapped when filling the system with water. A ruler was attached to the filter body to measure the height of the granular bed. The expansion process was recorded with a video camera (HDR-CX105E, Sony, Tokyo, Japan).

Two porous media were analysed: glass microspheres (Sovitec Belgium, Fleurus, Belgium) and silica sand (Sibelco Hispania, Bilbao, Spain). Both media were washed, dried and sieved to a narrow range prior to the experimental study. Their characteristics are listed in Table 1, where the equivalent diameter d_{eq} corresponded to the diameter of a sphere having the particle average volume of the porous media, the porosity ε was defined as the volume of voids divided by the

Table 1 – Main properties of the porous media used (from Bové et al., 2015).

Property	Units	Microspheres	Silica sand
Grain size range	(mm)	0.63–0.75	0.75–0.85
Equivalent diameter d_{eq}	(mm)	0.65	0.92
Sphericity coefficient ψ	(–)	1	0.89
Porosity ε	(–)	0.38	0.40
Particle density ρ_p	(kg m^{-3})	2436	2510

total volume occupied by the media (calculated with the particle density ρ_p and the porous media bulk density), and the sphericity coefficient ψ (≤ 1) was the division between the surface to volume ratio of the equivalent sphere to the actual surface to volume value (Bové et al., 2015). The product of the sphericity coefficient by the equivalent diameter equalled the Sauter mean diameter $d_p = \psi d_{eq}$, used as the mean particle diameter for the calculations carried out in the present work.

Data were obtained by gradually opening the inlet valve of the filter from its fully closed position. At each valve position, the volumetric flow rate was calculated by measuring the time needed to circulate 5 l. This process was repeated 3 times. The relative errors of the flow rate, and also of the mean superficial velocity, were below 4%. The granular bed height was measured from the ruler attached to the filter body when analysing the recordings (a minimum of 60 s with data extracted at 2 s intervals), though it was also annotated in-situ to validate the figures. The maximum opening of the discharge valve was empirically determined to avoid media losses due to an excess of the bed expansion (maximum superficial velocities of $v_s = 156$ m h^{-1} and 127 m h^{-1} for microspheres and silica sand media, respectively). The entire process was repeated twice, and the height measured at rest confirmed the assumption of non-relevant media losses in previous essays.

2.2. Model set up

2.2.1. Two-dimensional model

Simulations were carried out with ANSYS-Fluent 2020R1. This commercial CFD software had already been applied to simulate fluidised beds (Cornelissen, Taghipour, Escudié, Ellis, & Grace, 2007; Córcoles, Acosta-Iborra, Almendros-Ibáñez, & Sobrino, 2021). The multiphase Eulerian–Eulerian approximation was chosen, in which the granular phase was identified as a material that interacts with the flow with properties obtained from the kinetic theory (ANSYS, 2021). These simulations involve many formulations and parameters. The knowledge of the model response to changes in these various terms is essential to define the settings finally adopted. But the investigation of the consequences of changing many model parameters became unfeasible in the three-dimensional (3D) geometry of the filter due to limitations in computational resources. Therefore, efforts were originally focused on thoroughly analysing a very well documented two-dimensional (2D) case (Cornelissen et al., 2007). This 2D liquid–solid (water-sand) fluidised bed case included a comprehensive summary of the Eulerian–Eulerian model settings and reported experimental data for validation purposes (Cornelissen et al., 2007). The assessment of the results obtained in the 2D model enabled the 3D model to be set up.

The original model studied by Cornelissen et al. (2007) used a planar 2D geometry. Here, axisymmetric 2D cases with different grid sizes were also investigated (see Fig. 3) since were expected to better reproduce the real conditions. Thus, the boundary conditions in the 2D model were defined as in Fig. 3B. Another difference from Cornelissen et al. (2007) was the adoption of a more refined grid towards the wall boundaries to account for their effects on the main flow, since real 3D filters have complex elements (underdrains, diffusers, etc.)

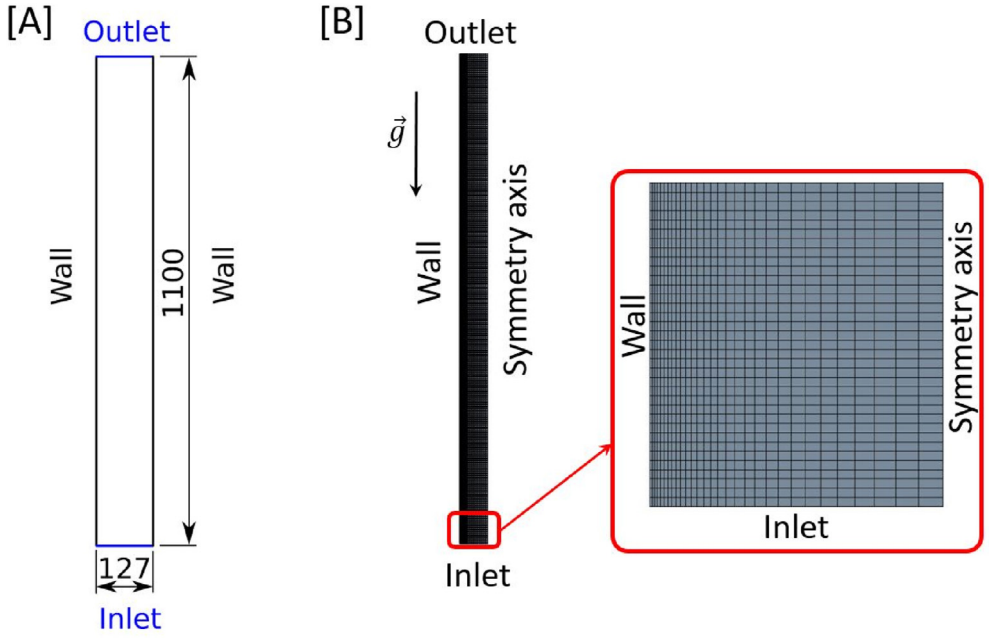

Fig. 3 – Dimensions of the 2D planar model of Cornelissen et al. (2007) (units in mm) with boundary types [A], and axisymmetric 2D model with a detailed view of the mesh near the inlet (case with 30 × 550 divisions) [B].

Table 2 – Multiphase model equations for the base model. Formulations proposed for different authors are described in detail in ANSYS Inc (2021).

Term	Units	Formulation/Value
Granular viscosity	Pa s	Syamlal and O'Brien
Granular bulk viscosity	Pa s	Lun et al.
Solid pressure	Pa	Lun et al.
Granular temperature	$m^2\ s^{-2}$	Algebraic
Frictional viscosity	Pa s	Schaeffer
Frictional Pressure	Pa	None
Angle of internal friction	°	30
Radial distribution		Syamlal and O'Brien
Drag Coefficient		Wen and Yu
Restitution coefficient		0.9

that require mesh refinements. For example, the mesh of 30 × 550 (horizontal × vertical) divisions in Fig. 3B had a bias factor of 10 with element dimensions ranging from 5.3 × 2 mm near the axis of revolution to 0.53 × 2 mm near the wall. A grid sensitivity study was carried out with four different meshes: 20 × 250, 25 × 400 and 30 × 550 divisions, and a full size 60 × 550 (i.e., as for geometry in Fig. 3A instead of the half cut Fig. 3B), all with a bias factor equal to 10. The grid convergence index (Roache, 1997) was calculated with the three axisymmetric meshes to estimate the error due to the discretization effect.

The main settings of the Eulerian–Eulerian formulation are detailed in Table 2. The model assumed uniform size particles with a diameter equal to the Sauter mean one ($d_p = \psi d_{eq}$). The use of a characteristic diameter in monodisperse media equations has provided reasonable results in CFD studies of pressurised filters with porous media having a reduced range of particle size distribution (see, e.g., Pujol et al., 2020). The effect of changing the radial distribution to the formulation of Lun et al. (ANSYS, 2021), the drag coefficient to the formulation of Huilin-Gidaspow, which is a combination of both Wen-Yu model and Ergun equation with a smooth switch between both formulations (ANSYS, 2021), and the specification of the granular temperature in terms of an algebraic equations instead of using a more comprehensive partial differential equation (ANSYS, 2021) were also investigated. All cases were unsteady with initial conditions at rest. For the base case, the time step was fixed to $\Delta t = 10^{-3}$ s, with $\Delta t = 10^{-2}$ s and 10^{-4} s conditions also tested. The transient formulation employed the first order implicit method. The pressure–velocity coupling scheme was the Phase Coupled SIMPLE. The spatial discretisation was chosen as second order for all variables, except for the volume fraction that used the QUICK algorithm. All simulations used 100 inner iterations and were run for a minimum flow time of 30 s in double precision. The convergence criteria fixed the threshold residuals to 10^{-3} for all variables, but results with this condition equal to 10^{-4} were also analysed. Superficial velocity values were fixed at the inlet and fell into the range of the experimental data published in Cornelissen et al. (2007) (45.4, 89.6, 137.2, 182.2, 227.5, 274.3, 320.0 and 360.0 m h^{-1}). Standard atmospheric pressure (101,325 Pa) was set at the outlet. Water properties corresponded to those at 12 °C (density $\rho_f = 999.5$ kg m^{-3} and viscosity $\mu = 1.23 \times 10^{-3}$ Pa s). The interaction between granular and water phases did not account for turbulence effects, explicitly ignoring the available turbulent options in the multiphase model. However, the water flow was defined as turbulent when the Reynolds number exceeded a threshold value. This numerical set up aimed to correctly represent the fluidised bed region (mainly in laminar or transitional conditions as seen in Sections 3 and 4), and the water-only region above (in turbulent conditions under some operational conditions). The latter definition was of particular interest to properly simulate the flow pattern at the small outlet in the 3D case (see Section 4). In the 2D case, the outlet had the same dimensions as the inlet in a straight column, so no major changes in the flow patterns due to turbulence were expected. Thus, by default, base case simulations used laminar conditions, though simulations with the shear stress transport $k-\omega$ (SST $k-\omega$) turbulence model at flow conditions with Reynolds number $Re = \rho_f v_s h/\mu > 2000$ with the 2D horizontal width $h = 127$ mm (Fig. 3) were also investigated. For comparison purposes, the porous media properties corresponded to those of the glass spheres employed in Cornelissen et al. (2007), being the initial height equal to 198 mm, the porosity of the packed bed $\varepsilon_0 = 0.4$, the particle density $\rho_p = 2540$ kg m^{-3} and the Sauter mean diameter $d_p = 1.13$ mm.

2.2.2. *Three-dimensional laboratory filter*

The fluidised bed in the 3D filter described in Fig. 2 was simulated with a quarter model by taking advantage of symmetry conditions. For simplicity, only the region above the perforated plate that supported the media was simulated. Five different grids were investigated whose main characteristics are detailed in Table 3 and shown in Fig. 4. Grids were labelled as R for real (Fig. 4A and B) and as M for modified (Fig. 4C–E) geometries, as explained later. Since the study aimed to propose recommendations for simulating the backwashing

Table 3 – Main characteristics of the meshes analysed: mesh type, characteristic element size, number of elements, ratio of nominal grid spacing to particle diameter $\Delta l/d_p$ (silica sand – microspheres), minimum orthogonal quality OQ_{min}, maximum aspect ratio AR_{max} and maximum value of the skewness S_{max}.

Case	Mesh type[a]	Element size (mm)	Number of elements	$\Delta l/d_p$	OQ_{min}	AR_{max}	S_{max}
R1	H + T	2	650,090	2.4–3.1	0.15	44	0.85
R2	T	1	3,345,987	1.2–1.5	0.15	19	0.85
M1	T	1	4,446,723	1.2–1.5	0.16	17	0.84
M2	T	1.6	1,384,143	1.9–2.4	0.18	18	0.82
M3	T	5	457,213	6.0–7.5	0.20	18	0.80

[a] H = Hexahedrons, T = Tetrahedrons.

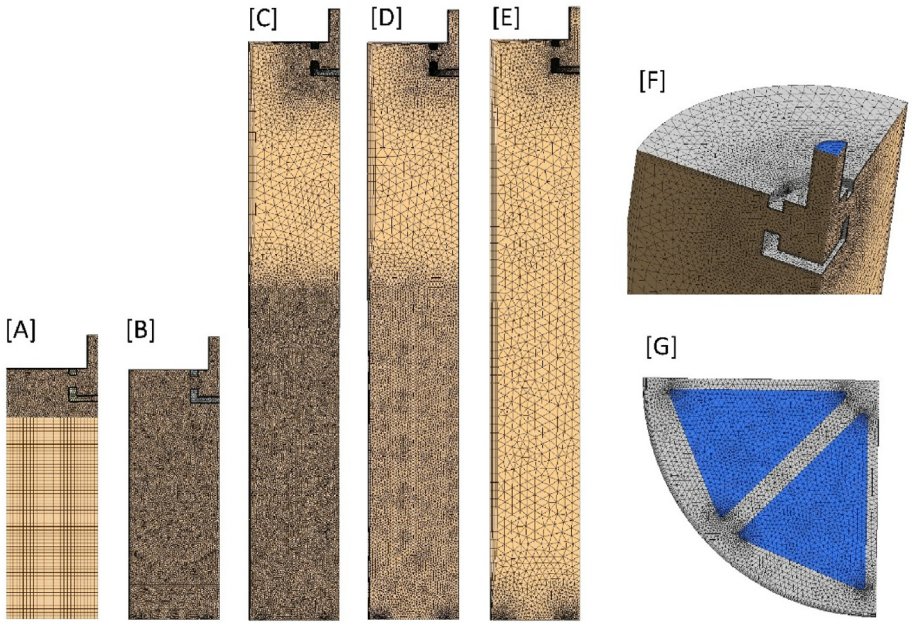

Fig. 4 – Vertical view of the grids for R1 [A], R2 [B], M1 [C], M2 [D] and M3 [E] meshes (see Table 3). For cases [B]–[E], details of the upper region [F] and of the bottom one [G], in which the water outlet and inlet boundaries are coloured in blue.

regime in commercial porous media filters, grids needed to ensure the correct representation of different accessories, such as diffusers and nozzles. Therefore, tetrahedral grids with inflation layers on the walls were chosen so these unstructured meshes successfully captured the flow behaviour in complex geometries. This contrasted with previous numerical studies that employed quadrilateral (2D) or hexahedral (3D) structured grids in simplified geometries (e.g., Córcoles et al., 2021; Cornelissen et al., 2007). Results with a hybrid grid, with a structured mesh (hexahedrons) at the lower domain and an unstructured mesh (tetrahedrons + prisms) at the upper one (region with the diffuser plate) were also obtained. In the Eulerian–Eulerian approximation, the element size depends on the constraints of the drag force closure relation, which requires a grid cell size Δl bigger than the particle size d_p (Shi, Komrakova, & Nikrityuk, 2019). All these grids satisfied this condition for the nominal values (Table 3), though near walls, $\Delta l / d_p \approx 0.5$ in the finest mesh due to the refinement at the inflation layer (as it also occurred in the 2D grid). However, it was assumed that this effect would be of minor importance, and preferred to correctly capture the flow behaviour near the walls. Grids labelled as M2 and M3 in Table 3 were used in order to evaluate the fine grid convergence index.

The Δl also influenced the time step fixed in the simulations. The Courant-Friedrichs-Lewy number $CFL = u\Delta t / \Delta l$, where u is a characteristic flow velocity, is recommended to be below 1 so as to improve the convergence of the simulations (Córcoles et al., 2021). In terms of the maximum value of the superficial velocity experimentally obtained, and with the characteristic element size for each mesh (Table 3), the following time steps satisfied the $CFL \leq 1$ condition: $\Delta t =$ 0.047 s for R1 case, and $\Delta t = 0.025$ s for R2 and M1-3 cases. However, following Córcoles et al. (2021), the time step for case R1 (hybrid mesh) was reduced to $\Delta t = 2.5 \times 10^{-4}$ s, with 40 inner iterations per Δt. The R2 case (finer mesh than R1) was intended to provide more accurate information of the position of the top layer of the fluidised bed. The simulation process followed four steps in which Δt was progressively increased to avoid instabilities: step 1) from rest (initial conditions) to 2 s: $\Delta t = 0.010$ s and 80 inner iterations per Δt, step 2) from 2 s to 3 s: $\Delta t = 0.015$ s and 60 inner iterations per Δt, step 3) from 3 s to 4 s: $\Delta t = 0.020$ s and 40 inner iterations per Δt, and step 4) from 4 s on: $\Delta t = 0.025$ s and 20 inner iterations per Δt. However, both R1 and R2 cases suffered from some simulation issues at high superficial velocities, in which part of the granular material was lost through the outlet. This was the reason for the M1 design (Fig. 4C) that used the finer mesh but a modified geometry which consisted in enlarging the main body 200 mm in comparison with the real filter body. Under this configuration, no loss of granular media at the outlet was observed using the less conservative values of $\Delta t = 0.025$ s and 20 inner iterations per Δt, as it had a faster simulation than the R2 case (a computational time in the order of 210 h per simulation required in an Intel Xeon W-2155 CPU with 128 GB of RAM running with 4 cores).

The model set up followed that detailed in the 2D above (as suggested from the sensitivity analysis carried out in Section 3). Boundary conditions were set as uniform velocity at the inlet (blue regions in Fig. 4G), atmospheric pressure at the outlet (blue region in Fig. 4F), symmetry at the two vertical cuts (Fig. 4A-E), and non-slip walls for all other surfaces. The water flow governing equations were set to laminar in those operating points in which the Reynolds number $Re = \rho_f v_s d_f / \mu$ was below 2000 (assumed to be the threshold value). For flows with larger Reynolds numbers, the Unsteady Reynolds Averaged Navier–Stokes $k-\omega$ turbulence model was employed though few simulations with the $k-\varepsilon$ (with standard wall

functions) turbulence model were also carried out with differences of the predicted expanded bed height <5%. As in the 2D case, the interaction between both granular and water phases ignored turbulence effects. Water properties were constant and equal to those at 20 °C.

2.3. Analytical approximations

The expansion of the granular bed height L_r relative to the initial value L_0 (no backwashing flow) was defined as

$$L_r(\%) = \frac{(L - L_0)}{L_0} 100 \tag{1}$$

where L is the height of the granular bed at a given backwash flow rate.

The L term is often evaluated from the mass conservation equation of the granular material, which is divided by the filter cross-sectional area A_f and the particle density ρ_p to obtain,

$$(1 - \varepsilon_0)L_0 = (1 - \varepsilon)L \tag{2}$$

where the left-hand side corresponds to the condition at rest, with known values of initial height L_0 and porosity ε_0, and the right-hand side refers to the condition at a given backwash flow rate, with both bed height L and porosity ε to be predicted.

The value of the expanded bed porosity ε has been estimated by several authors. Soyer and Akgiray (2009) obtained it from the expression

$$f = \frac{\varepsilon g(\rho_p - \rho_f) d_p}{\rho_f \left(\frac{v_s}{\varepsilon}\right)^2} \tag{3}$$

with f the dimensionless friction factor and g the acceleration of gravity. Note that the term v_s/ε is the mean local fluid velocity inside the granular media. Equation (3) multiplied by the square of the modified Reynolds number, defined as

$$Re_1 = \frac{d_p \rho_f v_s}{6\mu(1 - \varepsilon)} \tag{4}$$

is (see Soyer & Akgiray, 2009)

$$\varphi = f Re_1^2 = \frac{\varepsilon^3}{(1 - \varepsilon)^2} \frac{\rho_f d_p^3 g(\rho_p - \rho_f)}{216\,\mu^2} \tag{5}$$

Dharmarajah and Cleasby (1986) developed the following expression for the dimensionless group φ,

$$\varphi = 3.01\, Re_1 \text{ for } Re_1 < 0.2 \tag{6}$$

whereas Soyer and Akgiray (2009), after correlating with experimental data, proposed

$$\log \varphi = \log(3.137 Re_1 + 0.673 Re_1^{1.766}) - (0.930 + 0.274 \log Re_1)(-\log \psi)^{1.262} \tag{7}$$

which was expected to better represent the fluidised bed at high expansion regimes.

More recently, Kramer et al. (2020) proposed a new set of equations to improve the prediction of voidage in liquid–solid fluidised beds suitable for full-scale applications such as those found in drinking water treatment plants. These equations were able to take into account the fluidisation in laminar and transitional regimes where flow heterogeneity was observed. This heterogeneity arose not only in porous media with broad particle-size distribution, but also with spherical monodisperse glass beads (Kramer et al., 2020).

In terms of the modified particle Reynolds number,

$$Re_\varepsilon = \frac{d_p \rho_f v_s}{\mu(1 - \varepsilon)} \tag{8}$$

the complete turbulent flow regime is expected to emerge at $Re_\varepsilon > 2000$. Lower values corresponding to laminar and transitional flow regimes are found in most engineering liquid–solid fluidisation processes. The dimensionless drag coefficient for the laminar regime $f_L$can be expressed as a function of Re_ε and of the friction term for the turbulent regime f (Kramer et al., 2020),

$$f_L = f Re_\varepsilon \tag{9}$$

The substitution of Eq. (9) into Eq. (3), using Eq. (8) and rearranging terms, gives

$$g(\rho_p - \rho_f)(1 - \varepsilon) = f_L \frac{\mu}{d_p^2} \frac{(1 - \varepsilon)^2}{\varepsilon^3} v_s \tag{10}$$

which expresses the pressure drop per unit length through the fluidised bed. This hydraulic gradient behaves linearly with the superficial velocity for a constant value of f_L, as expected.

Kramer et al. (2020) pointed out that the particle Froude number, defined as

$$Fr_p = \frac{v_s}{\sqrt{\left(\frac{\rho_p}{\rho_f} - 1\right) g d_p}} \tag{11}$$

may become the relevant number to determine the fluidisation state in terms of homogeneous or heterogeneous flow patterns. Thus, these authors argued that the dimensionless factor f should not only incorporate the Re_ε (laminar – transitional – turbulent flow) number but also the Fr_p (homogeneous – heterogeneous flow) one. The most accurate model developed by Kramer et al. (2020) was called the Reynolds-Improved-Outlook model (RIO 1), where the dimensionless factor f was

$$f = \frac{c_1}{RF} + \frac{c_2}{RF^{c_3}} \tag{12}$$

with c_1, c_2, and $c_3$adjusted constants to experimental data and the Reynolds-Froude RF dimensionless parameter followed

$$RF = Re_\varepsilon \frac{\left(1 + c_4 Fr_p^{c_5}\right)}{\left(1 + c_6 Fr_p^{c_5}\right)} \tag{13}$$

with c_4, c_5, and $c_6$constants also obtained after fitting experimental data. Values equal to $c_1 = 150$, $c_2 = 12.2$, $c_3 = 0.244$, $c_4 = 18.9$, $c_5 = 1.43$, and $c_6 = 0.00903$ provided voidage predictions with an average relative error less than 1% (Kramer et al., 2020).

Thus, three estimates of the expanded bed height from previous developed models were reported here. These values were obtained from the solution of the expanded bed porosity ε that when substituted into Eq. (2) enabled L, and, consequently from Eq. (1), of the relative bed height L_r. Equation (5), using Eq. (6) or Eq. (7), was used to predict the expanded bed porosity ε for the Dharmarajah and Cleasby (1986) or the Soyer

and Akgiray (2009) models, respectively. Equation (10) using Eq. (12) substituted into Eq. (9) provided the expanded bed porosity ε values for the Kramer et al. (2020) RIO 1 model.

On the other hand, the expanded bed porosity ε can also be obtained by applying the Reynolds transport theorem to a control volume defined by the porous media, in which the buoyant force per unit cross-sectional area equals the pressure drop Δp along the bed column (McCabe et al., 1993),

$$g(\rho_p - \rho_f)(1-\varepsilon)\mathrm{L} = \Delta p \tag{14}$$

In an upward flow with no fluidisation, the pressure drop in Eq. (14) is equivalent to that in filtration mode, in which the Ergun equation successfully reproduces experimental data (Graciano-Uribe et al., 2021). In this case, Eq. (14) reads,

$$g(\rho_p - \rho_f)(1-\varepsilon) = 150\frac{\mu}{d_p^2}\frac{(1-\varepsilon)^2}{\varepsilon^3}v_s + 1.75\frac{\rho_f(1-\varepsilon)}{d_p\varepsilon^3}v_s^2 \tag{15}$$

where the first term on the right-hand side corresponds to the viscous resistance term, directly related to flow friction losses in the water channels formed inside the granular media, and the second term on the right-hand side refers to the inertial resistance, which is mainly affected by the minor losses arisen in the continuous changes of the cross-sectional area inside these water channels. Note that Eq. (10) corresponds to Eq. (15) but neglecting the v_s^2 term on the right hand side. Thus, a constant value of $f_L = 180$ reduces Eq. (10) to the Kozeny-Carman expression, being expected to be valid for laminar regimes with $Re_\varepsilon < 2$ (see, e.g., Graciano-Uribe et al., 2021).

The superficial velocity that initiates the fluidisation of the granular bed is called minimum fluidisation velocity $v_{s,min}$. It can be estimated from Eq. (15) with the initial bed porosity ε_0 (McCabe et al., 1993), forming the solution of the following expression,

$$g(\rho_p - \rho_f)(1-\varepsilon_0) = 150\frac{\mu}{d_p^2}\frac{(1-\varepsilon_0)^2}{\varepsilon_0^3}v_{s,min} + 1.75\frac{\rho_f(1-\varepsilon_0)}{d_p\varepsilon_0^3}v_{s,min}^2 \tag{16}$$

However, as fluidisation progresses, the tortuosity of the water channels inside the granular media reduces. In an idealised description of the process, water channels inside the porous media can be described in terms of cylinders of length L and diameter d_c such that their cylindrical surface areas equal the available particle surface areas. This condition implies that (see McCabe et al., 1993)

$$d_c = \frac{2}{3}\frac{\varepsilon}{(1-\varepsilon)}d_p \tag{17}$$

and, therefore, the pressure drop due to friction per unit channel length $\Delta p_f/\mathrm{L}$, following the Hagen–Poiseuille law (i.e. the first equality in Eq. (18)), can be written as

$$\frac{\Delta p_f}{\mathrm{L}} = \frac{32\mu}{d_c^2}\frac{v_s}{\varepsilon} = 72\frac{\mu}{d_p^2}\frac{(1-\varepsilon)^2}{\varepsilon^3}v_s \tag{18}$$

where the v_s/ε term is the velocity inside the water channel. Note that Eq. (18) could also be derived from the Darcy–Weisbach equation $f\rho_f v_c^2/(2d_c)$ applied to a water channel with the friction factor for laminar conditions $f = 64/Re_c$, being $Re_c = \rho_f d_c v_c/\mu$ the Reynolds number of the flow in the water channel and $v_c = v_s/\varepsilon$ the mean water channel velocity.

Equation (18) exclusively refers to flow friction losses, so it substitutes the first term on the right-hand side of Eq. (15), now being

$$g(\rho_p - \rho_f)(1-\varepsilon) = 72\frac{\mu}{d_p^2}\frac{(1-\varepsilon)^2}{\varepsilon^3}v_s + 1.75\frac{\rho_f(1-\varepsilon)}{d_p\varepsilon^3}v_s^2 \tag{19}$$

Note that Eq. (19) is essentially the same as Eq. (15) but substituting the 150 value by 72.

In the description of water channels as paths of length L, minor losses could be understood as a series representation of N sudden contractions plus expansions due to the geometry of the surrounding grain columns. Under this assumption, the pressure drop per unit length $\Delta p_m/\mathrm{L}$ related to minor losses follows

$$\frac{\Delta p_m}{\mathrm{L}} = \frac{\mathrm{N}}{\mathrm{L}}K\frac{\rho_f}{2}\frac{v_s^2}{\varepsilon^2} \tag{20}$$

with $K = 1.5$ being the addition of the loss coefficient of a sudden expansion plus that of a sudden contraction (White, 2009). The length L is related to the number of grains in a column N, so $d_pN = L$, and Eq. (14) can be expressed as

$$g(\rho_p - \rho_f)(1-\varepsilon) = 72\frac{\mu}{d_p^2}\frac{(1-\varepsilon)^2}{\varepsilon^3}v_s + K\frac{\rho_f}{2d_p}\frac{v_s^2}{\varepsilon^2} \tag{21}$$

which takes into account both major (Eq. (18)) and minor (Eq. (20)) contributions to the pressure drop per unit length.

The ability of the previous equations to predict the relative expansion of the bed height Eq. (1) was quantitatively evaluated using the root mean square error (RMSE)

$$RMSE = \sqrt{\frac{\sum_{i=1}^{n}\left(L_{ro,i} - L_{rc,i}\right)^2}{n}} \tag{22}$$

where $L_{ro,i}$ and $L_{rc,i}$ were the ith value of the L_r observed and calculated, respectively, and n was the total number of experimental data. An indicator of a good predictive capacity was the coefficient n_t, expressed as

$$n_t = \frac{SD}{RSME} - 1 \tag{23}$$

withSD the standard deviation of the experimental $L_{ro,i}$ values (Bové et al., 2015). In addition, the Nash-Sutcliffe efficiency coefficient (NSE) was also reported

$$NSE = 1 - \frac{\sum_{i=1}^{n}\left(L_{ro,i} - L_{rc,i}\right)^2}{\sum_{i=1}^{n}\left(L_{ro,i} - L_{ro,avg}\right)^2} \tag{24}$$

where $L_{ro,avg}$ was the average value of L_{ro}. Values of $n_t > 2.2$ and $NSE > 0.9$ indicated very good predictive capacity (Bové et al., 2015).

3. Two-dimensional model results

As an example of the two-dimensional simulations, Fig. 5 shows the volume fraction of the glass spheres (equal to one minus the expanded bed porosity) at different flow times using the base model formulation detailed in Table 2, with

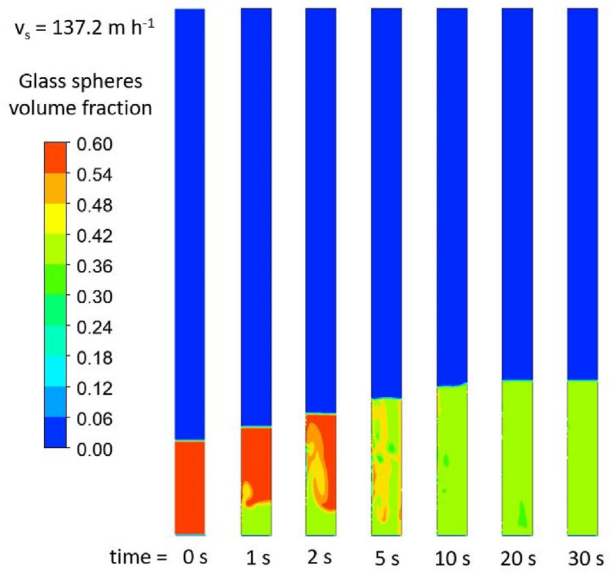

Fig. 5 – Time evolution of the volume fraction of glass spheres for the base case two-dimensional axisymmetric model with $v_s = 137.2$ m h^{-1}.

superficial velocity $v_s = 137.2$ m h^{-1}, reference mesh (30 × 550), time step $\Delta t = 10^{-2}$ s, SST $k-\omega$ turbulence model and residuals threshold at 10^{-3}. As observed in Fig. 5, there was a rapid expansion at the initial stages, with increased porosity at the symmetry axis, being similar to the patterns observed in Cornelissen et al. (2007). The expanded bed height remained almost steady after 10 s of simulation. This behaviour was common in the other superficial velocities analysed.

Reported steady values of bed porosity ε were obtained after computing the average value extracted in horizontal lines distributed at 20 mm intervals for the simulation with a flow time equal to 30 s. All lines in which $\varepsilon > 0.9$, or, equivalently, volume fraction of the granular material <0.1, were ignored. This threshold value was chosen as a yardstick to be applied in all cases with the purpose of being below the expected porosity at the maximum flow rate and, at the same time, not being low enough to produce false positives due to numerical inaccuracies. For a case with s = 92 m h^{-1}, the predicted bed layer height differed by less than 2% when this criterion was varied from 0.05 to 0.2 in terms of the volume fraction of the granular media. The height of the expanded bed was determined with a central vertical line applying the same threshold condition, and the results were verified to follow the conservation Eq. (2). Time averaged data were not required since in the 2D simulations the top layer of the fluidised bed remained almost perfectly steady beyond 20 s.

With the model set up used in Fig. 5 but with different superficial velocities, simulations provided a reasonable agreement with experimental data for moderate bed expansion values (<150% increase) at $v_s < 200$ m h^{-1} (Fig. 6).

As the bed expanded, the granular volume fraction diminished and the difference (in %) between predicted and measured bed height L became greater than the difference (in %) of the expanded bed porosity value ε. For example, differences between simulated and measured ε values were below 3.5% for the entire range of backwashing flow analysed. In contrast, the very same cases gave differences between the observed and estimated bed height by as much as 19.8% at the highest superficial velocity. In fact, from Eq. (2), relative errors related to the bed height L were in the order of $\varepsilon/(1-\varepsilon)$ times those of the bed porosity ε. Therefore, in situations with bed porosity $\varepsilon > 0.5$ (as in the majority of cases in Fig. 5), $\varepsilon/(1-\varepsilon) > 1$, and, therefore, the key variable to determine the model accuracy was L rather than ε.

Classical analytical expressions of L published by Soyer and Akgiray (2009) and by Dharmarajah and Cleasby (1986) provided reasonable estimates of measured data at $L_r <$ 150%, though they substantially overestimated the observations for large backwash flows. Results from the Kramer et al. (2020) model were of remarkable agreement with the experimental data for the entire range of superficial velocities, being the model with the highest prediction accuracy ($NSE = 1.00$ and $n_t = 3.73$). These efficiency indices were even higher than those of the simulated data. In contrast, the expansion bed

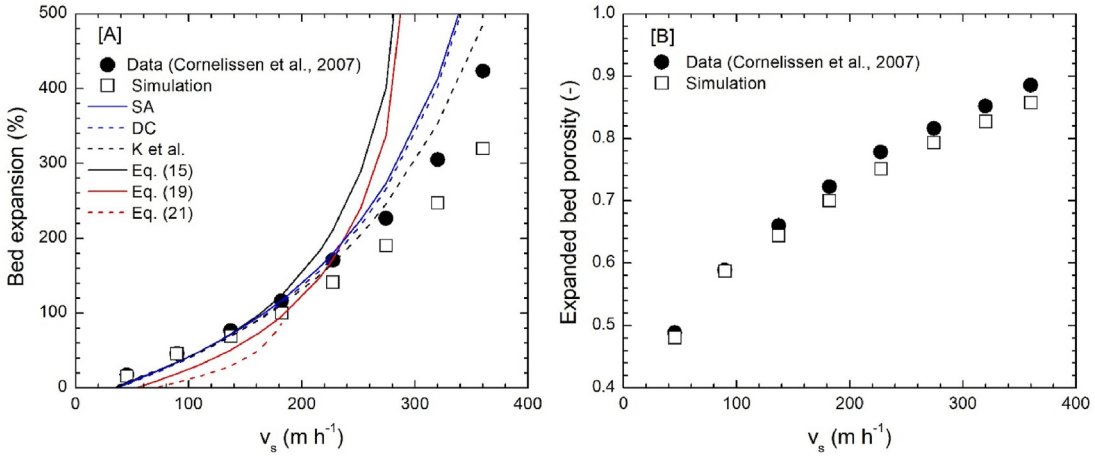

Fig. 6 – Simulated bed expansion L_r [A] and expanded bed porosity ε [B] at 30 s as a function of the superficial velocity of the two-dimensional case. Bed expansion predictions from analytical equations are also shown: SA stands for Soyer and Akgiray model, DC for Dharmarajah and Cleasby model, and K et al. for Kramer et al. RIO 1 model.

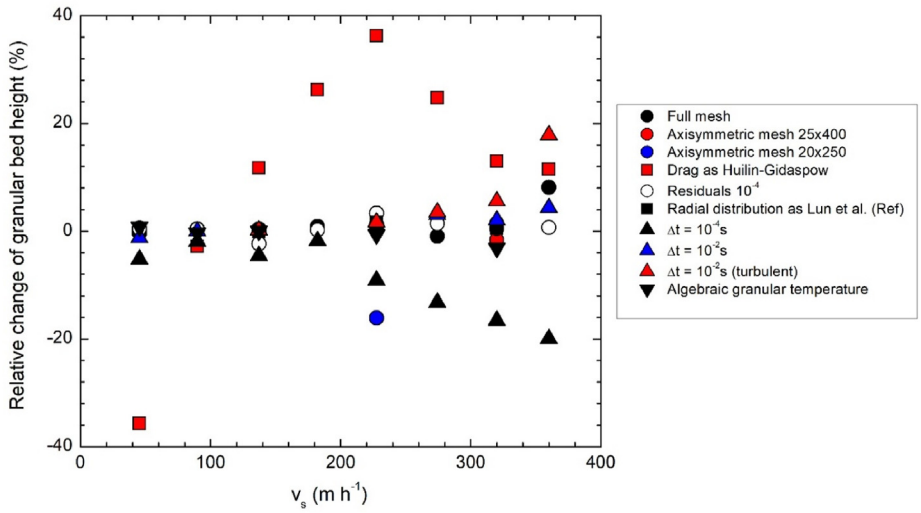

Fig. 7 – Change of the predicted granular bed height relative to that of the base case simulation (%) as a function of the superficial velocity for different model configurations.

model that applied the Ergun equation for estimating the hydraulic gradient Eq. (15), behaved similarly to the previous equations at moderate backwashing flow rates, but predicted unrealistically high bed expansions at high superficial velocities. In comparison, Eq. (19) gave a lower height for the granular bed since it included a head loss term per unit length of minor relevance. Thus, in comparison with Eq. (15), the expanded bed porosity in Eq. (19) should decrease (and so the expanded bed height) to enhance the pressure losses and, thus, to equal the net buoyant forces per unit area. The flow regime in the fluidised bed was mainly transitional, with $Re_e = 600$ at $v_s = 282$ m h^{-1}, though the water-only region above it was turbulent at lower superficial velocities (e.g., $Re = 3000$ at $v_s = 105$ m h^{-1}).

For comparison with the base case set up run with $\Delta t = 10^{-3}$ s and laminar conditions, the effect of changing different model configurations at the predicted height of the granular bed is shown in Fig. 7. The effect of adopting the turbulence model instead of the laminar one for the water flow was very low in the $v_s < 200$ m h^{-1} and bed expansions <150% range. Values of the expanded bed height were highly dependent on the drag model used. At low superficial velocities (45.4 m h^{-1}), the bed height using the Huilin-Gidaspow model was 36% shorter than that obtained with the Wen-Yu formulation. However, at higher superficial velocities (182.2 m h^{-1}), the Huilin-Gidaspow model predicted a longer expanded bed, with a height being 26% higher than with the Wen-Yu drag model (see Fig. 7). The latter result followed the trend found in Cornelissen et al. (2007) when changing the drag model at high backwashing flow rates. For moderate backwashing flow rates, in the range of those applied in pressurised porous media filters for micro-irrigation applications ($v_s < 200$ m h^{-1} and bed expansions <150%), most of the different set up conditions evaluated did not produce substantial changes in the predicted expanded bed height. However, as the superficial velocity increased, discrepancies were evident when using different Δt values, with a reduction of the simulated granular bed height as Δt decreased. The effect of reducing the mesh from 30 × 550 to 25 × 400 had minor effects. A further reduction to a 20 × 200 mesh had a greater impact due to the loss on the vertical spatial resolution (grid elements 4.4 mm high instead of 2.0 mm in the original mesh). The uncertainty due to the discretization was evaluated following the procedure detailed in Celik et al. (2008). The fine grid convergence index GCI^{21}_{index} varied depending on the flow rate. For a superficial velocity of 45.4 m h^{-1}, $GCI^{21}_{index} = 0.12\%$ with an apparent order of the approximation equal to $p = 1.8$. For a superficial velocity of 137.2 m h^{-1}, $GCI^{21}_{index} = 0.01\%$ with an apparent order of the approximation equal to $p = 7.0$, which was substantially greater than the theoretical order of the numerical solution (second order). However, high values of p have also been reported in similar processes (Koerich, Lopes, & Rosa, 2018).

As suggested from these results, and with the purposes of having fast and reliable simulations of the 3D filter experimentally tested, the 3D model set up was essentially defined the same as that of the 2D base case but with an algebraic granular temperature formulation, with a turbulence model when required, and with a different value of Δt (see details in Section 2.2.2).

4. Laboratory filter results

4.1. *Microspheres*

Laboratory observations clearly revealed an unsteady granular media pattern with a fairly unpredictable uneven top free surface, especially at high backwashing flow rates (see Fig. 8). The reason was mainly caused by a flow inlet that did not occupy the entire filter cross-sectional area (Fig. 4G), and was much more realistic than the homogeneous flow applied in the 2D case (Section 3). The non-uniform inlet flow along the filter cross-sectional area created different types of flow circulation patterns inside the granular media clearly visible through the transparent filter walls. At high backwashing flow rates, the top free layer of the expanded granular bed

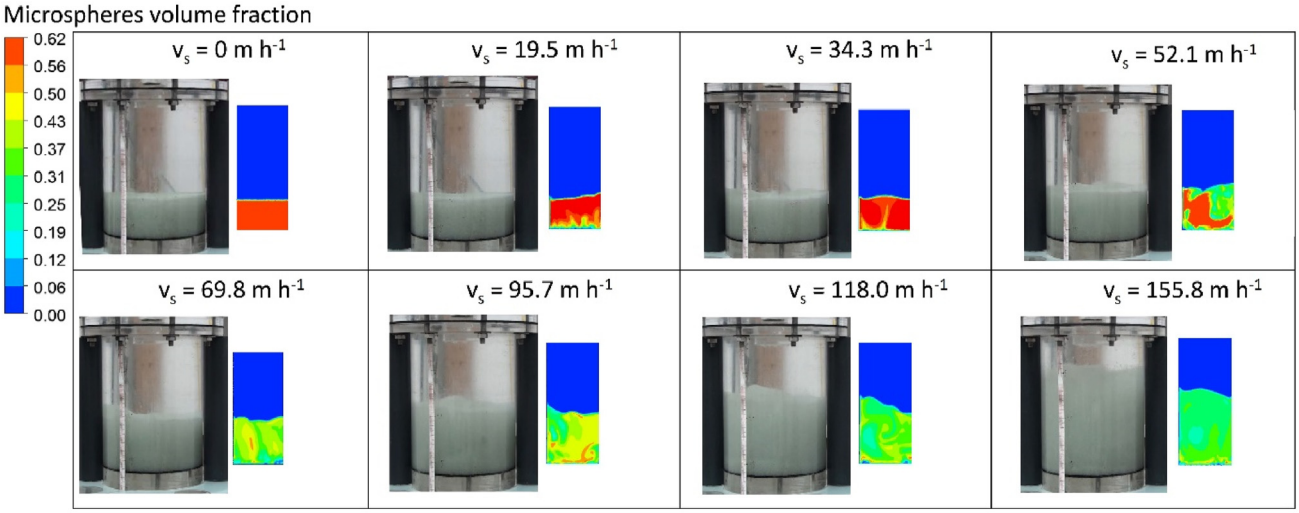

Fig. 8 – Simulated volume fraction of microspheres at the symmetry wall shown in Fig. 4C at flow time 50 s for different superficial velocities in comparison with the observed laboratory behaviour. The symmetry wall was a vertical plane whose width was the radius (see Fig. 4C).

exhibited an oscillatory behaviour. Therefore, the reported height of the granular bed did not correspond to a fixed flow time but to average values, as explained in the methodology section. The flow regime in the fluidised bed was clearly transitional, with $Re_\varepsilon = 192$ at $v_s = 180$ m h^{-1}, though the water-only region above reached $Re = 5000$ at this superficial velocity.

Simulations with the M1 configuration also developed an uneven top layer of the granular material that fluctuated depending on time. Selected qualitative results of the volume fraction at the symmetry wall at 50 s flow time are shown in Fig. 8, being compared with a representative image of the laboratory recording. Numerical results clearly indicated a non-uniform concentration of microspheres inside the expanded bed, varying both radially and vertically (and also angularly, which was not detectable in Fig. 8). The homogeneity of the microspheres concentration was high at very low flow rates (due to a very mild flow almost unable to sustain the media) and, also, at very high ones (due to a vigorous flow that favoured mixing).

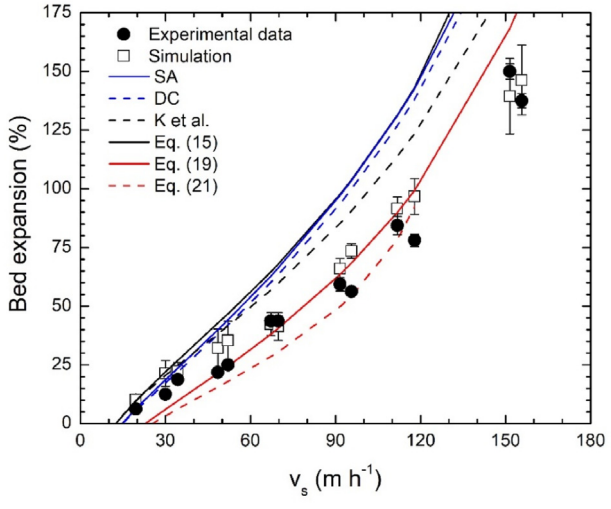

Fig. 9 – Microspheres bed expansion as a function of the superficial velocity for laboratory data, simulations and analytical equations (SA stands for Soyer and Akgiray model, DC for Dharmarajah and Cleasby model, and K et al. for Kramer et al. RIO 1 model). Error bars correspond to twice the standard error.

Quantitative numerical results of the granular volume fraction were collected in five vertical lines located at a radial distance equal to 55 mm from the axis of rotation and separated from each other by 22.5°. This radial distribution allowed the analysis of two vertical lines above the inlet flow region plus three vertical lines above the reinforcement walls (that were effectively treated as two vertical lines, since data of the two lines, 0° and 90°, lying at both symmetry walls were averaged). The vertical coordinate where the granular volume fraction decreased to a value < 0.1 (bed porosity >0.9) was identified as the expanded bed height. The average value of this height from 20 s to 50 s flow time simulation, taken at 1 s interval, for the effective four vertical lines was used to determine the expanded bed height of the simulation - in Fig. 9, where error bars refer to twice the standard error of simulated data (approximately 95% confidence interval). Note that, in general, the predicted expanded bed height had a remarkable agreement with the observations.

Since the 2D case showed a clear dependence on the type of the drag model applied, results with the Huilin-Gidaspow model instead of the Wen-Yu one were also obtained. In general, the Huilin-Gidaspow model predicted a higher bed, increasing by 10%, 9%, 13% and 7% the values simulated by applying the Wen-Yu model at superficial velocities of 30.0 m h^{-1}, 67.2 m h^{-1}, 95.7 m h^{-1} and 118.0 m h^{-1}, respectively. This trend was also observed in the 2D case, though there the Huilin-Gidaspow model predicted lower bed heights for superficial velocities below 90 m h^{-1} approximately. The choice of the drag model here used (Wen-Yu in Figs. 8–11) was based on previous successful CFD applications (Cornelissen et al., 2007) that here reasonable reproduced the

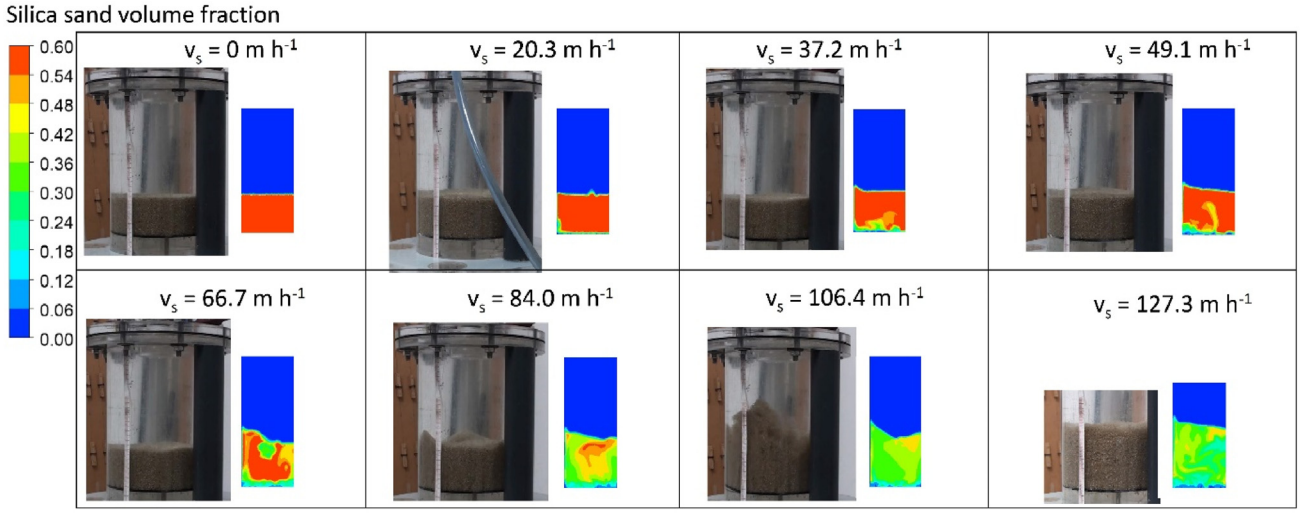

Fig. 10 – Simulated volume fraction of silica sand at the symmetry wall shown in Fig. 4C at flow time 50 s for different superficial velocities in comparison with the observed laboratory behaviour. The symmetry wall was a vertical plane whose width was the radius (see Fig. 4C).

experimental measurements. It must be pointed out that the development of a suitable drag model for CFD simulations of a solid–liquid fluidization process is an area of ongoing research. Recently, for example, formulations of drag models directly proportional to the particle Reynolds number have successfully reproduced experimental results of liquid–solid fluidised bed tapered bioreactors (Koerich et al., 2018).

On the other hand, the uncertainty related with the discretization process was evaluated with M1, M2 and M3 meshes at two different superficial velocities. At $v_s = 91.7$ m h^{-1}, the $GCI^{21}_{index} = 0.3\%$ with an apparent order of the approximation equal to $p = 6.4$, whereas at $v_s = 118.0$ m h^{-1}, the $GCI^{21}_{index} = 6.0\%$ with an apparent order of the approximation equal to $p = 2.0$. These errors were below those reported from the variability of the data series of the simulated height.

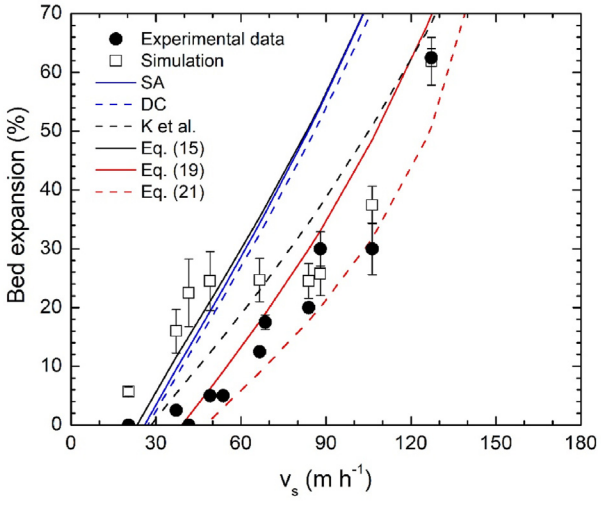

Fig. 11 – Silica sand bed expansion as a function of the superficial velocity for laboratory data, simulations and analytical equations (SA stands for Soyer and Akgiray model, DC for Dharmarajah and Cleasby model, and K et al. for Kramer et al. RIO 1 model). Error bars correspond to twice the standard error.

Classical analytical equations tended to overestimate the observed bed expansion values, with the predictions of the equations of Soyer and Akgiray, Eq. (7), and Dharmarajah and Cleasby, Eq. (6), almost matching the simple control volume approximation with the Ergun equation (Eq. (15)). This effect was also observed in Fig. 6, but was not noticeable then since the flow rate span more than doubled that of Fig. 9 and the differences were broader in the high superficial velocities region. In comparison, the Kramer et al. RIO 1 model, Eq. (10), improved the bed expansion prediction, though slightly overestimating its value. The new expression Eq. (19) correctly reproduced the trend observed, whereas its modified version, Eq. (21), could not manage the upper range of flow rates since it generated unrealistic expanded bed porosity values (>1). Equation efficiency indicator values of $NSE > 0.88$ and $n_t > 2.1$ were obtained for Eq. (19), and were higher than those of the other equations analysed ($NSE < 0.60$ and $n_t < 0.63$, for the RIO 1 model). The fact that, in contrast with the 2D case, Eq. (19) better represented both observations and simulations than Eqs. (6) and (7) is discussed in Section 5, where more data are provided.

4.2. *Silica sand*

Silica sand employed in the experimental analyses had greater density and longer Sauter mean diameter than microspheres (see Table 1). Therefore, the downward net buoyant force per particle (weight minus buoyancy) had a greater magnitude than that of microspheres. As a consequence, the fluidisation of this granular material was not as easy to occur as in Fig. 9. Thus, high momentum values at the inlet were required to expand the media (compare Figs. 8 with 10). Nevertheless, once fluidised, the behaviour of the expanded bed was similar to that observed for the microspheres, with an uneven free surface fluctuating with time.

This confirmed that the origin of such behaviour was caused by the experimental layout of the filter rather than by the media used. Unfortunately, higher superficial velocity values than those reported were not investigated since they damaged the flat rubber gasket of the inner plunger that sustained the draining screen.

Experimental data pointed out that incipient fluidisation began as late as $v_s \approx 50$ m h^{-1} (Fig. 11). Simulations reproduced the observed trend for $v_s > 70$ m h^{-1}. For lower superficial velocities, the numerical model systematically overestimated the bed expansion, highlighting the difficulty in correctly simulating the incipient fluidisation process. Indeed, two different trends were observed for the CFD results in Fig. 11, one corresponding to simulations that used the laminar formulation for the water flow ($v_s < 65$ m h^{-1}, $Re < 2000$), and another to those applying the turbulence model for the water flow ($v_s > 65$ m h^{-1} and $Re > 2000$). However, the adoption of the turbulence model for the regimes with low superficial velocities did not substantially improve the predicted bed expansion value. In terms of the fluidised bed, all cases were clearly in the transitional regime ($Re_\varepsilon < 82$). It was noted that the inherent discretisation of the domain may account for a 2.5% uncertainty in the results, and was more relevant in a media with low expansion. This difference between outputs of both laminar and turbulent models was not so evident in microspheres since there was a larger bed expansion there (comparing Fig. 9 with Fig. 11).

On the other hand, analytical equations verified one of the conclusions extracted with the analysis of microspheres: output values of the expanded bed height from Eqs. (6), (7) and (15) were almost indistinguishable in our range of study. In comparison, Kramer et al., RIO 1 model, Eq. (10), remarkably improved the bed expansion prediction, and as also observed for Eqs. (19) and (21), better followed the measured and simulated trends. In this case, Kramer et al. RIO 1 model and Eq. (19) matched the efficiency indicator values, ($NSE = 0.92$ and $n_t = 2.95$), being the highest of all models and providing a very good predictive capacity.

Regarding simulations, all previous data were obtained with the M1 geometry (see Fig. 4C) since with the R2 model configured as explained in Section 2, it was observed that 1) flows with low Reynolds numbers (laminar conditions) had serious numerical instabilities, and 2) flows with high Reynolds numbers discharged a portion of the granular media through the outlet. All these problems disappeared using the modified M1 geometry. For those cases in which the simulation with the R2 model was successful, differences in the predicted height of the expansion bed between the R2 and the M1 models were smaller than 13%, always being higher for the R2 case.

Finally, results with the hybrid mesh case R1 compared with those of the M1 always predicted a shorter bed expansion, ranging almost monotonically from −2% to −28% as the backwash flow increased. This behaviour was aligned with the finding of the 2D case (Fig. 7), where coarser meshes predicted lower expanded beds. In this configuration, numerical issues similar to those encountered in the R2 case were also observed, which led to the decision to employ the M1 model.

5. Discussion

5.1. *Minimum fluidisation velocity*

The minimum fluidisation velocity $v_{s,min}$ obtained from Eq. (16) was 12.2 m h^{-1} for microspheres and 23.2 m h^{-1} for silica sand. These values were, in effect, the intersection of Eq. (15) with the *x*-axis in Figs. (9) and (11), respectively. By only taking into account the linear term in $v_{s,min}$ of Eq. (16), as in McCabe et al. (1993), values were 12.7 m h^{-1} (microspheres) and 25.6 m h^{-1} (silica sand), up to 10% higher in comparison with those from Eq. (16). Experimental data indicated that the fluidisation process began at 15 m h^{-1} and 30 m h^{-1} approximately for microspheres and silica sand. Thus, previous analytical expressions were confirmed as reasonable estimators of the minimum fluidisation velocity.

5.2. *Pressure drop*

The backwashing regime in porous media filters, as with those used in micro-irrigation, is a recurrent process repeated to clean retained particles off the granular bed. Therefore, the backwashing mode requires pumping power that may compromise the overall energy efficiency of the irrigation system. The hydraulic power P_h required to sustain the target flow rate Q can be calculated from $P_h = \Delta pQ$ with Δp the pressure drop in the entire filter.

Simulations indicated that the pressure drop through the fluidised bed was a small value in comparison with that of the total filter (Fig. 12 for microspheres). The main contribution to head losses corresponded to the outlet region, due to the effect of the diffuser plate, and to the reduction of the cross-sectional area from the inner filter to the exit pipe. As expected, the pressure drop in these accessories was proportional to v_s^2 and this trend dominated the entire pressure drop.

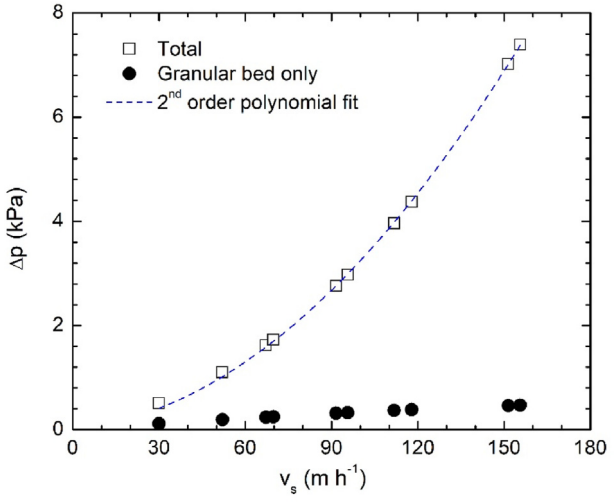

Fig. 12 – Pressure drop for the entire filter domain and for the granular bed as a function of the superficial velocity. Results are from the simulations of the microspheres cases.

In Fig. 12, a second order polynomial fit of pressure drop data with a fixed intercept at the origin achieved a R^2 value of 0.999. A similar behaviour was observed when using silica sand as a porous media. Thus, proposals of new diffuser and/or pipe-filter connection designs focused on reducing the energy demand should be analysed not only in filtration mode but especially in backwash since in the latter regime these accessories have predominant effects in the total pressure drop.

5.3. *Commercial filters*

In order to investigate the scope of the previous analytical equations, data recently published by de Deus, Mesquita, Salcedo Ramirez, et al. (2020) were analysed. These authors carried out a comprehensive study of the backwash regime in three different commercial sand filters used in micro-irrigation. Filter 1 (F1) had a diameter of 400 mm and used 4 packed-disc units as underdrains. Filter 2 (F2) had a diameter of 500 mm and used 8 pod-type underdrains. Finally, filter 3 (F3) had a diameter of 750 mm and used 22 wand-type underdrains. In each one of these filters, de Deus, Mesquita, Salcedo Ramirez, et al. (2020) conducted experiments with three different initial heights of the granular bed (i.e., those measured with no flow), designated as: low H1, intermediate H2, and high H3. These were H1 = 150, 110 and 120 mm, H2 = 300, 225 and 235 mm, and H3 = 450, 340 and 350 mm for filters F1, F2, and F3, respectively. The porous media was silica sand in three different particle size ranges: G1 (range 0.5–1.0 mm), G2 (range 0.8–1.2 mm), and G3 (range 1.0–1.5 mm). For each one of these filters (3), initial heights (3) and porous media (3) combinations, the authors experimentally measured the expanded bed height as a function of the superficial velocity, up to a maximum value in the order of 250 m h^{-1}, though most of the results were below 150 m h^{-1}. In terms of the Reynolds number, the operational conditions varied from $2425 \leq Re \leq 33705$, which implied a turbulent flow in the water-only region. However, regarding the modified particle Reynolds number, values were situated in the $6.2 \leq Re_\varepsilon \leq 355.8$ range, corresponding to a fluidised bed in a transitional regime.

The analytical expressions developed in Section 2.3 were applied to all cases of the previous work by assuming a Sauter mean diameter equal to the particle mid-range value for each porous media (i.e., 0.75 mm for G1, 1.00 mm for G2, and 1.25 mm for G3), a value of the packed bed porosity equal to $\varepsilon_0 = 0.40$, and a silica sand density equal to 2510 kg m^{-3}, as these were common values for this type of media (e.g., Table 1). In addition, water properties at 19 °C were considered, as this was the mid temperature of the water temperature range reported in the experiments (de Deus, Mesquita, Salcedo Ramirez, et al., 2020). Note that the expanded bed porosity value in Eqs. (6), (7), (10), (15), (19) and (21) was independent of the granular bed height L. Therefore, predicted bed expansion heights expressed in % of the initial value, as in Eq. (1), were exactly the same for all filter types F and heights H, only varying as a function of the characteristics of the porous media used.

Thus, data from de Deus, Mesquita, Salcedo Ramirez, et al. (2020) were grouped by particle size and compared with analytical equations (Fig. 13). For a given porous media, the expanded bed height as a function of the superficial velocity followed a common trend for all commercial filters, though cases with the lowest amount of granular media in the wand-type filter tended to have a larger bed expansion. This was probably due to the difference in the flow pattern exiting the wand-type underdrain F3 in comparison with that of the packed-disc F1 and pod-type F2 underdrains. In both F1 and F2 filters, the backwashing flow exited the underdrain in a predominantly upward direction. However, in the F3 filter, some of the backwash flow had a downwards direction exiting the

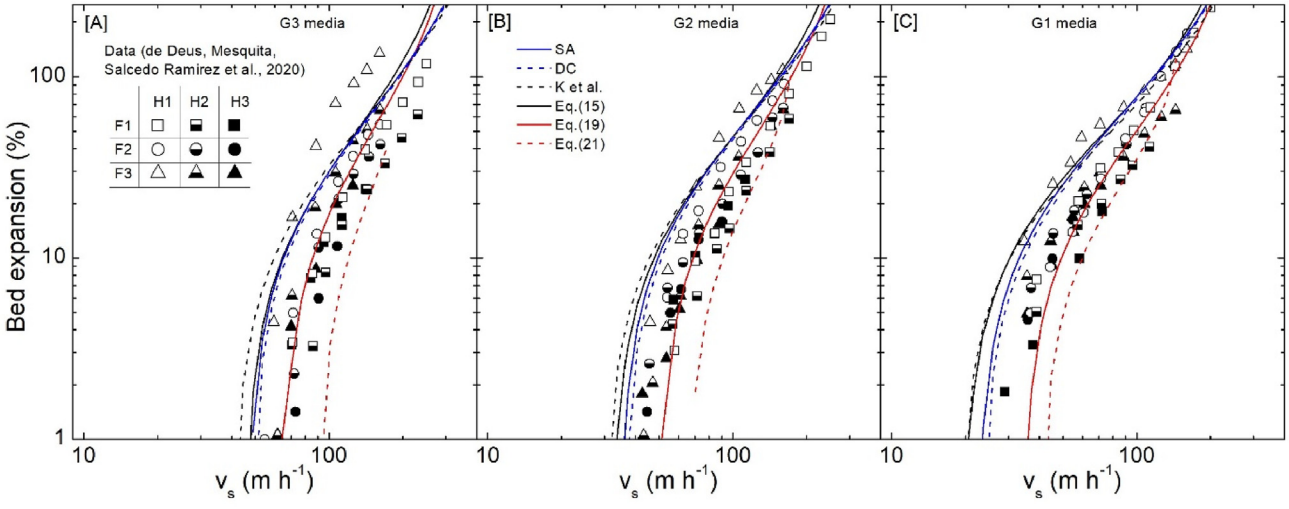

Fig. 13 – Bed expansion as a function of the superficial velocity predicted by different analytical expressions (SA stands for Soyer and Akgiray model, DC for Dharmarajah and Cleasby model, and K et al. for Kramer et al. RIO 1 model) for all cases studied in de Deus, Mesquita, Salcedo Ramirez, et al. (2020). F1, F2 and F3 were different commercial filters. H1, H2 and H3 were different initial heights (i.e., flow at rest) of the granular bed. The size of the porous media varied from large G3 [A], intermediate G2 [B], and low G1 [C]. See text for details.

wands and this may have modified the flow pattern inside the filter body, especially in shallow granular beds.

In agreement with the experimental results detailed in Section 4, it was found that 1) Eqs. (15), (7) and (6) slightly overestimated the expanded bed height, 2) Eq. (19) better reproduced the observed bed expansion trend for values approximately below 50%, and 3) Eq. (10) (Kramer et al. RIO 1 model) tended to better represent the measurements for higher values of bed expansion, in which Eq. (19) overestimated them, particularly when big grain sizes (>1 mm) were used in the filter. For all bed expansions, the equation efficiency indicators for Eq. (19) were $NSE = 0.38$ and $n_t = 0.28$ (G3 media), $NSE = 0.78$ and $n_t = 1.12$ (G2 media), and $NSE = 0.92$ and $n_t = 2.61$ (G1 media). In comparison, Kramer et al. RIO 1 model gave $NSE = 0.42$ and $n_t = 0.32$ (G3 media), $NSE = 0.75$ and $n_t = 1.01$ (G2 media), and $NSE = 0.87$ and $n_t = 1.77$ (G1 media), which indicated better predictions than Eq. (19) for G3 media and almost equal for G2 one. On the other hand, Dharmarajah and Cleasby Eq. (6) reported $NSE = 0.45$ and $n_t = 0.36$ (G3 media), $NSE = 0.74$ and $n_t = 0.97$ (G2 media), and $NSE = 0.83$ and $n_t = 1.48$ (G1 media), which were slightly better than those for Soyer and Akgiray Eq. (7), but clearly below those from Kramer et al. RIO 1 model and Eq. (19). The worst efficiency indicators were achieved by Eq. (15) for all cases ($NSE = 0.10$ and $n_t = 0.06$ for G3 media, $NSE = 0.37$ and $n_t = 0.27$ for G2 media, and $NSE = 0.73$ and $n_t = 0.95$ for G1 media), confirming the findings in Kramer et al. (2020) that the Ergun model loses accuracy as the Reynolds number increases. For individual initial heights and media, the best efficiency indicators were obtained with Kramer et al. (2020) RIO 1 model for the H1 height and G1 media case, achieving $NSE = 0.96$ and $n_t = 4.26$.

The results for porous media G2 and G1 (as well as those for the experimental cases in Section 4) opposed to those found in Section 3, where for the 2D case, Eqs. (6), (7) and (10) showed a better agreement than Eq. (19). This might have occurred due to the fact that the 2D case employed a granular media with a large particle size, and, from Fig. (13) and efficiency indicators above, Eqs. (6), (7) and (10) tended to approach the observations as the media G increased in size. Another fact to be considered is the difference in the flow pattern between the 2D uniform inlet/outlet case and the more constrained 3D plus commercial filter cases, in which both inlet and outlet flows were clearly non-uniform due to constructive geometrical changes (thus producing relevant pressure drops, as discussed in the previous subsection). The latter effect could be responsible for a slight inhibition of the bed expansion in comparison with what there would have been for unrestricted inlet/outlet domains.

Finally, an interesting result was that Eq. (21) could be understood as a lower bound of the expanded bed height value since, for all cases analysed (3D and Fig. 13), it predicted a reasonable approximation of the minimum height reached by the fluidised bed.

6. Conclusions

The backwashing regime in a laboratory pressurised granular media filter was analysed. Similar to commercial units, the upward flow at the filter inlet did not occupy the entire filter cross-sectional area, and the outlet region had a diffuser plate situated before the exit pipe. The expanded bed height L and its porosity ε were obtained from experiments, numerical models and analytical equations. The work was focused on moderate bed expansion values (<150%) since these are typical for commercial porous media filters in micro-irrigation due to constructive constraints. In most of the cases tested, the flow regime was turbulent in the water-only region though the fluidised bed was in a transitional regime.

The experiments exhibited an uneven expanded bed free surface with continuous variations at high flow rates. This was likely to be a consequence of the non-uniform flow past the inlet. CFD numerical simulations applied the Eulerian–Eulerian method, which was very demanding in terms of computational resources. A simplified 2D version correctly reproduced published data up to $v_s < 200$ m h^{-1}. The correct simulation of the expanded bed height L was more challenging than that of its porosity ε. For the 3D laboratory filter model, grids tested were a compromise between the mesh refinement to capture the flow details in filter accessories, and the minimum recommended mesh size in order to exceed the mean particle diameter. Numerical instabilities occurred when the Courant-Friedrichs-Lewy number (CFL) > 1. For conditions with $CFL < 1$, high backflow rates led to porous media losses through the outlet in models with the shortest filter body, even using 60 internal iterations per Δt. In comparison, the predicted expanded bed height L was remarkably similar to observations for developed fluidisation using a filter model with a longer body, with only 20 internal iterations per Δt, and $\Delta t = 0.025$ s. However, this configuration should use a fine mesh as otherwise it will tend to underestimate the expanded bed height values. In regimes with incipient fluidisation, simulations overestimated the expanded bed height, especially for the silica sand case. In addition, results presented important variations depending on the drag model adopted. Thus, the CFD model setup for the backwash mode in pressurised filters remains a complex task that requires validation on a case-by-case basis.

The classical analytical equations of Soyer and Akgiray (2009), and Dharmarajah and Cleasby (1986) correctly reproduced the results of the 2D uniform case for $v_s < 200$ m h^{-1}. However, these expressions systematically overestimated the bed expansion values measured in the laboratory filter. By comparison, the analytical RIO 1 model proposed by Kramer et al. (2020) showed a very good predictive capacity for both the 2D case (even superior to the CFD results) and 3D laboratory filter cases, though in the latter it slightly overestimated the bed expansion for small size microspheres. The analytical equation developed in this work also had a very good predictive capacity for the experimental data, though clearly failed at high expansion regimes (>200%) for large grain size media (2D case). The validity of this new analytical expression for porous media with mean particle diameter less or equal than 1 mm was underpinned with its application to external data published by de Deus, Mesquita, Salcedo Ramirez, et al. (2020). Finally, another new analytical equation was observed to provide a lower bound of the expanded bed height, and is suggested as being a useful approach for determining the minimum height reached by the granular media at a given backflow value.

Declaration of competing interest

The authors declare that they have no known competing financial interests or personal relationships that could have appeared to influence the work reported in this paper.

Acknowledgements

The authors would like to express their gratitude to Spanish Research Agency and the European Regional Development Fund for their financial support through Grant RTI2018-094798-B-100.

REFERENCES

Amirtharajah, A. (1971). *Optimum expansion of sand filters during backwash*. PhD dissertation. Ames, USA: Iowa State University.

ANSYS Inc. (2021). *ANSYS fluent theory guide*. Canonsburg, PA, USA: ANSYS Inc.

Bové, J., Arbat, G., Duran-Ros, Pujol, T.,M., Velayos, J., Ramírez de Cartagena, F., et al. (2015). Pressure drop across sand and recycled glass media used in micro irrigation filters. *Biosystems Engineering, 137*, 55–63. https://doi.org/10.1016/j.biosystemseng.2015.07.009

Brouckaert, B. M. (2004). *Hydrodynamic detachment of deposited particles in fluidised bed filter backwashing*. PhD dissertation. Atlanta, USA: Georgia Institute of Technology.

Burt, C. (2010). *Hydraulics of commercial sand media filter tank used for agricultural drip irrigation. ITCR Report No. R 10001*. San Luis Obispo, CA, USA: Irrigation Training and Research Center.

Celik, I. B., Ghia, U., Roache, P. J., Freitas, C. J., Coleman, H., & Raad, P. E. (2008). Procedure for estimation and reporting of uncertainty due to discretazation in CFD applications. *Journal of Fluids Engineering, 130*(7), Article 078001. https://doi.org/10.1115/1.2960953

Clements, M., & Haarhoff, J. (2005). Filter media expansion during backwash: The effect of biological activity. *Water SA, 30*(5), 51–55.

Córcoles, J. I., Acosta-Iborra, A., Almendros-Ibáñez, J. A., & Sobrino, C. (2021). Numerical simulation of a 3-D gas-solid fluidised bed: Comparison of TFM and CPFD numerical approaches and experimental validation. *Advanced Powder Technology, 32*, 3689–3705. https://doi.org/10.1016/j.apt.2021.08.029

Cornelissen, J. T., Taghipour, F., Escudié, R., Ellis, N., & Grace, J. R. (2007). CFD modelling of a liquid-solid fluidised bed. *Chemical Engineering Science, 62*, 6334–6348. https://doi.org/10.1016/j.ces.2007.07.014

de Deus, F. P., Mesquita, M., Salcedo Ramirez, J. C., Testezlaf, R., & de Almeida, R. C. (2020). Hydraulic characterisation of the backwash process in sand filters used in micro irrigation. *Biosystems Engineering, 192*, 188–198. https://doi.org/10.1016/j.biosystemseng.2020.01.019

de Deus, F. P., Mesquita, M., Testezlaf, R., de Almeida, R. C., & de Oliveira, H. F. E. (2020). Methodology for hydraulic characterisation of the sand filter backwashing processes used in micro irrigation. *MethodsX, 100962*(1–10). https://doi.org/10.1016/j.mex.2020.100962

de Deus, F. P., Testezlaf, R., & Mesquita, M. (2016). Assessment methodology of backwash in pressurized sand filters. *Revista Brasileira de Engenharia Agrícola e Ambiental, 20*(7), 600–605. https://doi.org/10.1590/1807-1929/agriambi.v20n7p600-605

Dharmarajah, A. H., & Cleasby, J. L. (1986). Predicting the expansion behavior of filter media. *Journal of the American Water Works Association, 78*(12), 66–76. https://doi.org/10.1002/j.1551-8833.1986.tb02768.x

Duran-Ros, M., Solé-Torres, C., Ait-Mouheb, N., Molle, B., Arbat, G., & Puig-Bargués, J. (2021). Media filter fouling assessment using optical coherence tomography: New methodology. *Biosystems Engineering, 204*, 26–35. https://doi.org/10.1016/j.biosystemseng.2021.01.008

Fatih Isik, M., Sönmez, Y., Yilmaz, C., Özdemir, V., & Nurcan Yilmaz, E. (2017). Precision irrigation system (PIS) using sensor network technology integrated with IOS/Android application. *Applied Sciences, 7*(1–14), 891. https://doi.org/10.3390/app7090891

Garb, Y., & Friedlander, L. (2014). From transfer to translation: Using systematic understandings of technology to understand drip irrigation uptake. *Agricultural Systems, 128*, 13–24. https://doi.org/10.1016/j.agsy.2014.04.003

Graciano-Uribe, J., Pujol, T., Puig-Bargués, J., Duran-Ros, M., Arbat, G., & Ramírez de Cartagena, F. (2021). Assessment of different pressure drop-flow rate equations in a pressurized porous media filter for irrigation systems. *Water, 13*(1–26), 2179. https://doi.org/10.3390/w13162179

Hua, L., Lu, L., & Yang, N. (2020). Effects of liquid property on onset velocity of circulating fluidisation in liquid-solid systems: A CFD-DEM simulation. *Powder Technology, 364*, 622–634. https://doi.org/10.1016/j.powtec.2020.01.051

Jiao, Y., Feng, J., Liu, Y., Yang, L., & Han, M. (2020). Sustainable operation mode of a sand filter in a drip irrigation system using Yellow River water in an arid area. *Water Supply, 20*(8), 3636–3645. https://doi.org/10.2166/ws.2020.217

Jorda-Capdevila, D., Gampe, D., Huber García, V., Ludwig, R., Sabater, S., Vergoñós, L., et al. (2019). Impact and mitigation of global change on freshwater-related ecosystem services in Southern Europe. *Science of the Total Environment, 651*, 895–908. https://doi.org/10.1016/j.scitotenv.2018.09.228

Koerich, D. M., Lopes, G. C., & Rosa, L. M. (2018). Investigation of phases interactions and modification of drag models for liquid-solid fluidized bed tapered bioreactors. *Powder Technology, 339*, 90–101. https://doi.org/10.1016/j.powtec.2018.07.102

Kramer, O. J. I., de Moel, P. J., Padding, J. T., Baars, E. T., Rutten, S. B., Elarbab, A. H. E., et al. (2021). New hydraulic insights into rapid sand filter bed backwashing using the Carman-Kozeny model. *Water Research, 197*(1–12), Article 117085. https://doi.org/10.1016/j.watres.2021.117085

Kramer, O. J. I., Padding, J. T., van Vugt, W. H., de Moel, P. J., Baars, E. T., Boek, E. S., et al. (2020). Improvement of voidage prediction in liquid-solid fluidized beds by inclusion of the Froude number in effective drag relations. *International Journal of Multiphase Flow, 127*(1–13), Article 103261. https://doi.org/10.1016/j.ijmultiphaseflow.2020.103261

Martos, V., Ahmad, A., Cartujo, P., & Ordoñez, J. (2021). Ensuring agricultural sustainability through remote sensing in the era of agriculture 5.0. *Applied Sciences, 11*(1–26), 5911. https://doi.org/10.3390/app11135911

IPCC. (2021). *Summary for policymakes. In V. Masson-Delmotte, P. Zhai, A. Pirani, S. L. Connors, C. Péan, S. Berger, et al. (Eds.), Climate change 2021: The physical science basis. Contribution of working group I to the sixth assessment report of the intergovernmental panel on climate change*. Cambridge: Cambridge University Press.

McCabe, W. L., Smith, J. C., & Harriott, P. (1993). *Unit operations of chemical engineering* (5th ed.). New York: McGraw-Hill, Inc.

Peng, J., Sun, W., Han, H., & Xie, L. (2021). CFD modeling and simulation of the hydrodynamics characteristics of coarse coal particles in a 3D liquid-solid fluidised bed. *Minerals, 11*(1–15), 569. https://doi.org/10.3390/min11060569

Pujol, T., Puig-Bargués, J., Arbat, G., Duran-Ros, M., Solé-Torres, C., Pujol, J., et al. (2020). Effect of wand-type underdrains on the hydraulic performance of pressurised sand media filters. *Biosystems Engineering, 192*, 176–187. https://doi.org/10.1016/j.biosystemseng.2020.01.015

Roache, P. J. (1997). Quantification of uncertainty in computational fluid dynamics. *Annual Review of Fluid Mechanics, 29*, 123–160. https://doi.org/10.1146/annurev.fluid.29.1.123

Schewe, J., Heinke, J., Gerten, J., Haddeland, I., Arnell, N. W., Clark, D. B., et al. (2014). Multimodel assessment of water scarcity under climate change. *Proceedings of the National Academy of Sciences, 11*(8), 3245–3250. https://doi.org/10.1073/pnas.1222460110

Shi, H., Komrakova, A., & Nikrityuk, P. (2019). Fluidised beds modeling: Validation of 2D and 3D simulations against experiments. *Powder Technology, 343*, 479–494. https://doi.org/10.1016/j.powtec.2018.11.043

Solé-Torres, C., Puig-Bargués, J., Duran-Ros, M., Arbat, G., Pujol, J., & Ramírez de Cartagena, F. (2019). Effect of underdrain design, media height and filtration velocity on the performance of microirrigation sand filters using reclaimed effluents. *Biosystems Engineering, 187*, 292–304. https://doi.org/10.1016/j.biosystemseng.2019.09.012

Soyer, E., & Akgiray, O. (2009). A new simple equation for the prediction of filter expansion during backwashing. *Journal of Water Supply: Research & Technology - Aqua, 58*(5), 336–345. https://doi.org/10.2166/aqua.2009.090

White, F. M. (2009). *Fluid mechanics* (7th ed.). New York: McGraw-Hill, Inc.

Zou, H., Fan, J., Zhang, F., Xiang, Y., Wu, L., & Yan, S. (2020). Optimization of drip irrigation and fertilization regimes for high grain yield, crop water productivity and economic benefits of spring maize in Northwest China. *Agricultural Water Management, 230*(1–11), 105986. https://doi.org/10.1016/j.agwat.2019.105986